Research Article

Hechuan Song, Hanjun Gao*, Qiong Wu and Yidu Zhang

Residual stress relief mechanisms of 2219 Al–Cu alloy by thermal stress relief method

https://doi.org/10.1515/rams-2022-0019
received October 08, 2021; accepted January 14, 2022

Abstract: Monolithic thin-wall components of 2219 Al–Cu alloy are widely used in aerospace and military fields, and usually treated with solution and quenching to improve their comprehensive performance. However, a high magnitude residual stress is introduced into the components during the quenching process, which is unfavorable to the subsequent manufacturing process and service performance. Therefore, residual stress relief is essential to enhance the performance of the components. A conventional effective method is thermal stress relief (TSR). However, the underlying mechanisms of TSR still remain unclear and lack a quantitative interpretation. In the present work, the evolution and distribution laws of the residual stresses, tensile properties, Vickers hardness, dislocations, precipitated phases, and metallography during TSR were investigated. Based on the experimental results, dislocation theory and strengthening mechanisms were applied to reveal the underlying mechanisms of the residual stress relief by TSR. The results showed that the circumferential and axial residual stress relief rates can reach 86.37 and 85.77% after TSR, respectively. The residual stress relief after TSR is attributed to the dynamic evolution of dislocation configuration and density. The improvement in the mechanical properties mainly depends on the precipitated phases and is also affected by the stress orientation effect caused by the residual stress.

Keywords: 2219 Al–Cu alloys, thermal stress relief, residual stresses, dislocations, mechanisms

*** Corresponding author: Hanjun Gao,** State Key Laboratory of Virtual Reality Technology and Systems, School of Mechanical Engineering and Automation, Beihang University, Room B313, New Main Building, Beijing, 100191, People's Republic of China; Anhui HengLi Additive Manufacturing Technology Co. LTD., Wuhu, 241200, People's Republic of China, e-mail: hjgao@buaa.edu.cn
Hechuan Song, Qiong Wu, Yidu Zhang: State Key Laboratory of Virtual Reality Technology and Systems, School of Mechanical Engineering and Automation, Beihang University, Beijing, 100191, People's Republic of China

1 Introduction

Due to the excellent high and low-temperature mechanical properties, high fracture toughness, strong stress corrosion resistance, and sound welding performance, the heat-treatable 2219 Al–Cu alloys are widely used in aerospace and military fields [1,2]. To obtain excellent mechanical properties, the heat-treatable 2219 Al–Cu alloys are generally quenched into cold water after solution treatment. However, an inevitable detrimental residual stress is produced in 2219 Al–Cu alloy components during the quenching process due to the severe thermal gradients [3,4]. In the subsequent machining process of these components, the balance state of residual stress in the components is broken with the removal of materials, and the residual stress is released and redistributed, causing vulnerable distortion and deteriorating dimensional accuracy, especially for large-scale and complex monolithic thin-walled components with low stiffness [5–7]. This stress also affects the static strength, stress corrosion, fatigue resistance, and dimensional stability during the service process, which greatly reduces the service life and safety performance of the components [8–11]. Therefore, how to effectively predict, control, and reduce the residual stress for improving the comprehensive performance of the components is highly valued in aerospace and other industrial fields.

At present, there are many methods for relieving residual stress in engineering. The essence of residual stress relief is to input energy into the atomic lattice of materials by applying external load such as force [12–14], heat [15–26], electricity [27–29], or magnetism [30–32], so that the elastic strain energy stored in the materials can be gradually relieved through micro- or local-plastic deformation [33–35]. Thermal stress relief (TSR) is the most widely used residual stress relief method at present. This method is to heat the components with a heating furnace and control the temperature drop after holding for a period of time, so as to reduce and homogenize the residual stress. To avoid introducing new residual stresses, the cooling rate should be properly controlled. The current relatively complete mechanism of residual stress relief by

TSR is that high temperature reduces the yield strength of the material, and the plastic deformation of the material will be caused when the internal stress exceeds the yield strength.

As an effective stress relief technology, TSR has gradually attracted the attention of scholars [15–22]. Bruno et al. [15] studied the residual stress distribution and microscope changes in the metal matrix composites after T6 and over-aging treatment by means of neutron diffraction. Epp et al. [16] investigated cold rolled rings and machined rings in terms of residual stress relaxation behavior during heating. They found that the residual stress of the two ring types decreases in varying degrees, and the differences in the initial residual stress state result in a different relaxation behavior. According to Kim et al. [17], the reduction percentages of the residual stresses of the high-density polyethylene pipe increases with increase in the annealing time and temperature. Younger and Eckelmeyer [18] compared the quenching process, mechanical deformation treatment, and thermal aging treatment to adjust the residual stress state of a heat-treated Al alloy satellite box, and the results showed that the thermal aging treatment reduced the residual stress magnitude by 40%.

However, the current research on TSR has primarily focused on the effectiveness of stress relief, rather than the underlying mechanisms of stress relief. There is no recognized mechanism of residual stress relief by TSR, or theoretical basis in practical applications. To reveal the underlying mechanisms of TSR, the effect of TSR on residual stress relief was evaluated and validated, and the evolution and distribution laws of microstructures and mechanical properties were then investigated in this study. After analyzing the experimental results, this study established the underlying mechanisms of TSR based on dislocation theory and strengthening mechanisms. The findings provide valuable insight into the underlying mechanisms of TSR and are an important reference for exploring the innovative heat-treatment process.

2 Materials and methods

2.1 Materials and TSR treatment

The experimental materials came from a large hot-rolled transition ring for a launch vehicle of 2219 Al–Cu alloy with an external diameter of 5 m, and the chemical composition of the alloy is listed in Table 1. Test pieces were cut from the ring for heat treatment, as shown in Figure 1a. Test pieces had a dimension of 45 mm (radial direction; RD) × 150 mm (axial direction; AD) × 450 mm (circumferential direction; CD). The heat treatment process involved solution treatment at 535°C for 150 min, and quenching in water at 25°C. Next piece 1 remained quenched as the original state (as-quenched; AQ) and piece 2 was subjected to TSR at 175°C for 2 h using a self-made stress relief experiment furnace (Figure 1b). The steps of this TSR involves heating the piece to 175°C in 0.5 h, then preserving for 2 h, and finally cooling with the furnace to room temperature.

2.2 Evaluation of residual stresses

The residual stress was measured using Prism manufactured by the Stresstech Group of Finland in this study. Prism is an advanced residual stress measurement device based on the hole-drilling method and electronic speckle pattern interferometry technique [36], as shown in Figure 2. Compared with the traditional hole drilling technique with strain gauges, Prism is simpler to operate without pasting the strain gauge, collects more data points, and calculates more reliable results. A carbide tool with a diameter of 1.6 mm was used in the experiment with a cutting speed of 5,000 rpm. The measured depths of each point were 0.1, 0.2, 0.4, 0.6, 0.8, and 1.0 mm, and the measuring points of the two test pieces are shown in Figure 1c.

2.3 Mechanical properties and microstructures

The evolution of mechanical properties and microstructure was examined to gain a better understanding of the internal mechanisms of TSR. The tensile samples with a total length of 100 mm and a thickness of 2.5 mm were cut from the central areas of the test piece, as shown in Figure 1c. The tensile test was performed at room temperature with a loading rate of 2 mm·min^{-1} using an INSTRON5967 universal testing machine, and the mechanical properties

Table 1: Chemical composition (wt%) of the 2219 Al–Cu alloy rings

Cu	Mn	Ti	Zr	V	Mg	Zn	Fe	Si	Al
5.8–6.8	0.2–0.4	0.02–0.1	0.1–0.25	0.05–0.15	≤0.02	≤0.1	≤0.3	≤0.2	Bal.

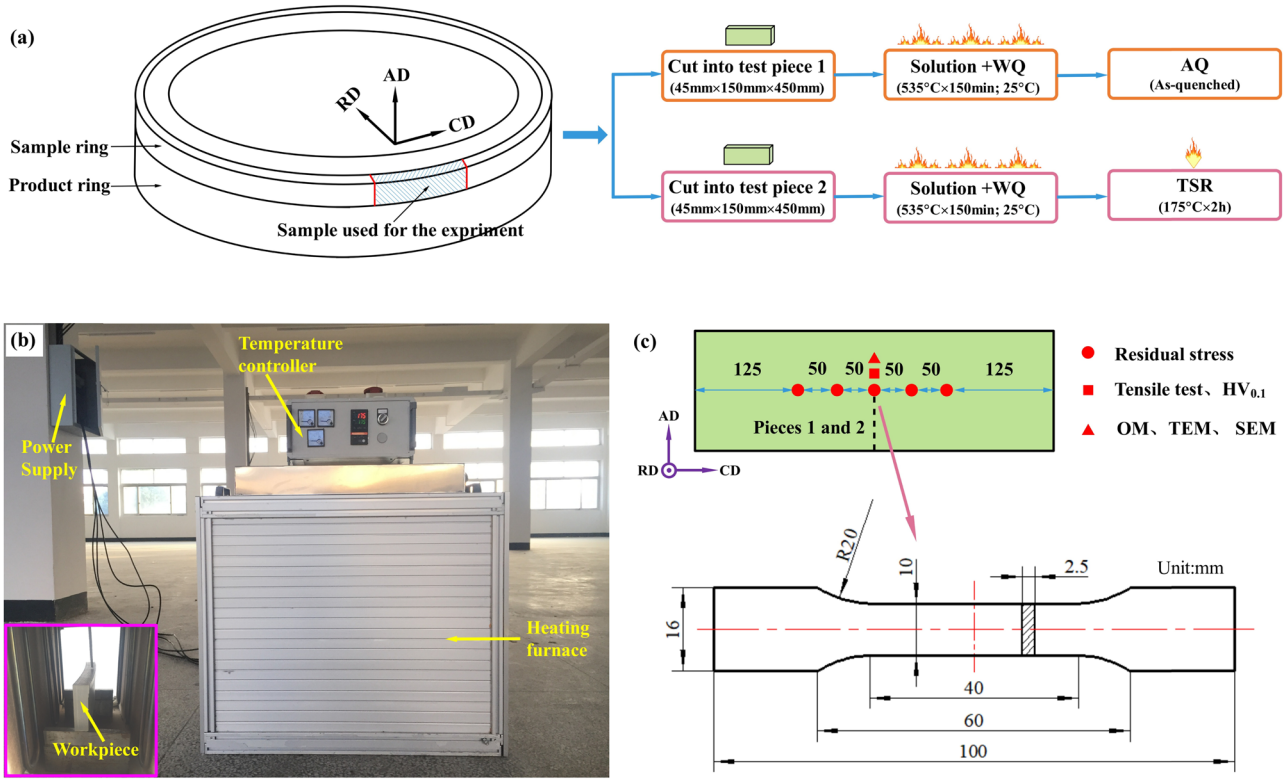

Figure 1: TSR experiments and sampling location maps: (a) sampling and various processing routes, (b) experimental equipment of TSR, and (c) measurement location and tensile sample maps. The dot in the direction icon indicates that RD is perpendicular to the paper surface and outward.

along the CD were examined. Each tensile test was repeated at least two times. Then, the fracture surfaces of the tensile samples were further examined in detail by a scanning electron microscope (SEM; JSM-7610FPlus). Hardness measurement was conducted by using the TUKON2500 Vickers hardness instrument at a load of 0.1 kg for a 10 s duration. Nine points were measured and averaged for each sample. The dislocations and precipitated phases were observed by a transmission electron microscope (TEM; Talos F200X G2). The samples were prepared by mechanical grinding with a thickness of 50–60 nm. Then, disks of Φ3 mm diameter were punched, and TEM foils were thinned by a twin-jet electropolishing device using a solution of 33% perchloric acid and 67% methanol with the electricity of 50–60 mA at −45 to −35°C. The metallographic microstructures were observed by optical microscopy (OM; ZEISS Observer Scope

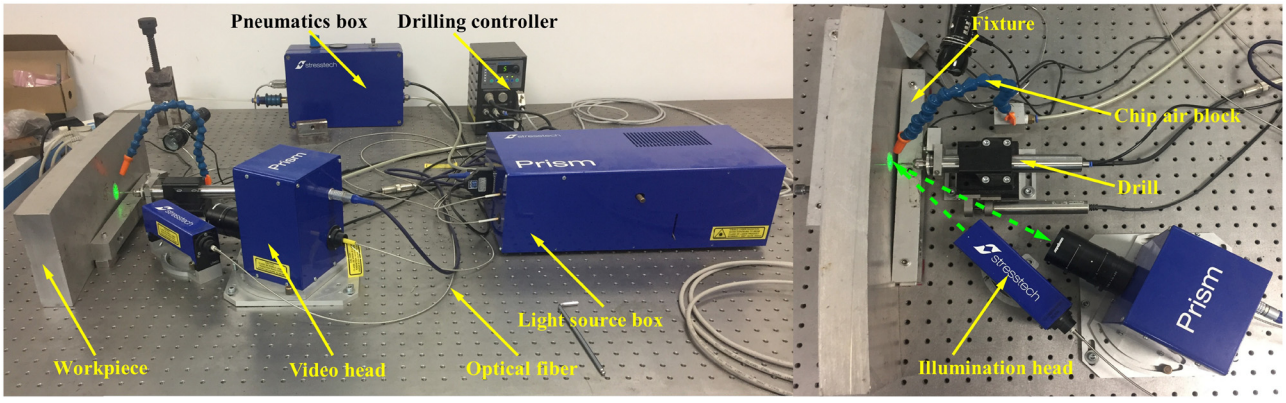

Figure 2: Residual stress measuring equipment.

A1m), and the samples were prepared by mechanical polishing and then anodically coated using the mixed liquor of 38% sulfuric acid, 43% phosphoric acid, and 19% water at 25 V per 0.17 A for 50 s.

3 Results

3.1 Residual stresses

The comparison curve of residual stresses along the depth direction between the AQ piece and the TSR piece is presented in Figure 3, in which the residual stress value of each layer depth is the average value of residual stresses of five measuring points. It can be seen from Figure 3 that the residual stresses first decreased, next increased and then decreased along the depth direction, reaching the maximum at 0.2 or 0.4 mm and the minimum at 0.8 mm. The residual stresses of the AQ piece are very large and fluctuate violently due to a large temperature gradient caused by the extremely uneven temperature. Compared with the value of the AQ piece, the value of circumferential residual stress decreased from −116.11 to −15.83 MPa, with a rate of 86.37% (Figure 3a); the value of axial residual stress decreased from −87.35 to −12.43 MPa, with a rate of 85.77% (Figure 3b). Therefore, the residual stress of the TSR piece decreased to a similar degree in both the CD and AD. Further, compared with the value of the AQ piece, the value of maximum principal stress decreased from −73.51 to −6.19 MPa, with a rate of

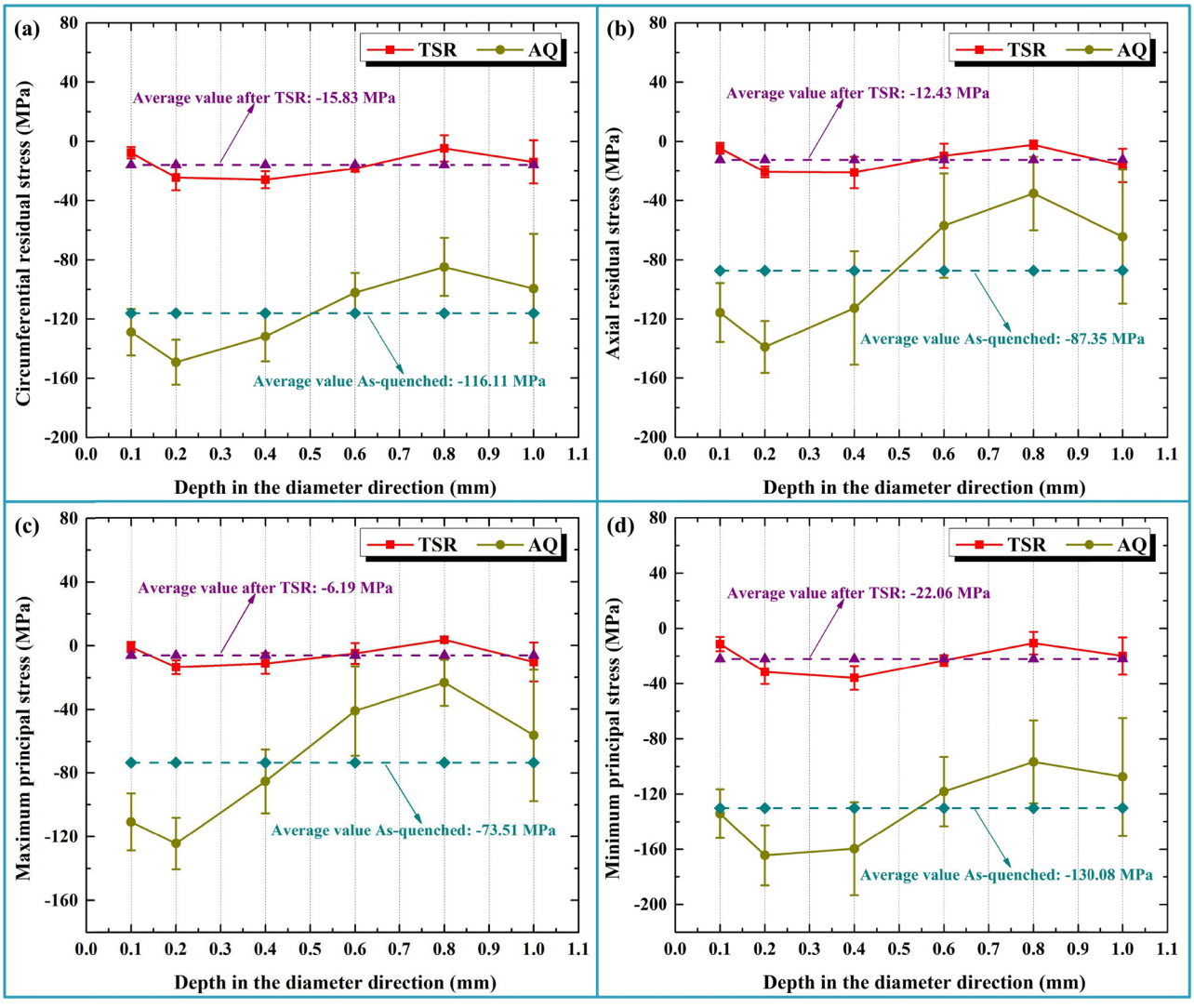

Figure 3: Comparison of residual stress distribution along the depth between the AQ piece and the TSR piece: (a) circumferential residual stress, (b) axial residual stress, (c) maximum principal stress, and (d) minimum principal stress.

91.58% (Figure 3c); the value of minimum principal stress decreased from −130.08 to −22.06 MPa, with a rate of 83.04% (Figure 3d). Therefore, the decrease in the maximum principal stress after TSR is greater than that of the minimum principal stress.

Figure 4 shows the ranges and average standard deviations of residual stresses of the AQ piece and the TSR piece. It can be seen from Figure 4 that compared with the value of the AQ piece, the ranges and average standard deviations of residual stresses after TSR decreased in different degrees. The maximum range value decreases from 103.74 to 17.23 MPa, and the maximum average standard deviation value decreases from 30.25 to 8.00 MPa. This smaller range and average standard deviation indicate that the residual stress distribution of the TSR piece was more uniform.

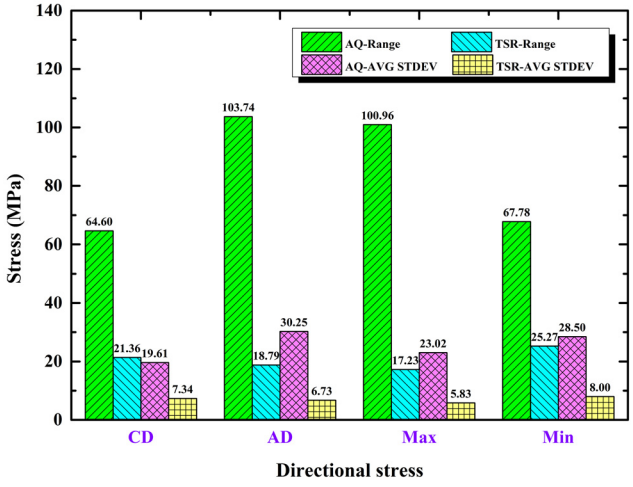

Figure 4: Comparison of ranges and average standard deviations of residual stresses between the AQ piece and the TSR piece. (1) CD: circumferential residual stress, (2) AD: axial residual stress, (3) Max: maximum principal stress, and (4) Min: minimum principal stress.

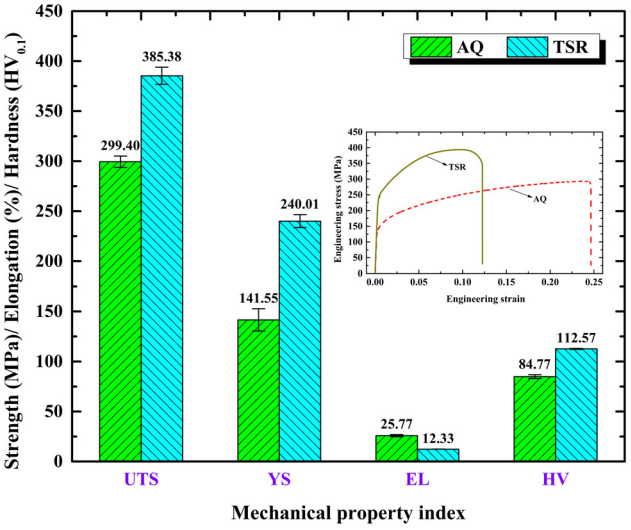

Figure 5: Comparison of tensile properties and Vickers hardness between the AQ piece and the TSR piece.

3.2 Mechanical properties and fracture behavior

Figure 5 shows the comparison of tensile properties and Vickers hardness between the AQ piece and the TSR piece. The distribution of and variation in the ultimate tensile strength (UTS), yield strength (YS), and Vickers hardness ($HV_{0.1}$) of the two pieces were similar. The UTS, YS, and $HV_{0.1}$ of the TSR piece were higher than those of the AQ piece by 85.98 MPa, 98.46 MPa, and 27.8 $HV_{0.1}$, respectively. However, the elongation (EL) of the TSR piece was lower than that of the AQ piece with a decrease by 13.38%.

To further study the effect of TSR on the mechanical properties, the tensile fracture surface using SEM was analyzed, as shown in Figure 6. A large number of big (elliptical frame) and tiny (rectangular frame) dimples were observed in the fracture morphology (Figure 6a1–b2), which indicate that the main fracture mode was microporous aggregation ductile fracture, and the existence of a large number of dimples indicate remarkable plasticity. Compared with the AQ piece (Figure 6a1 and a2), the TSR piece showed fewer dimples with a shallow depth, staggered and uneven size, and emergence of dark gray areas, which indicate that the increase in strength led to the decrease in the proportion of ductile fracture. This result was consistent with the results of tensile samples. In addition, the energy dispersive spectroscopy (EDS) spectrum in Figure 6c shows that the long strip phase A contained Al, Cu, Fe, and Mn, which can be determined as a mixture of Al_7Cu_2Fe and $Al_{20}Cu_2Mn_3$, and that the block phase B mainly contained Al and Cu, which can be determined as Al_2Cu. These two phases increased the stress concentration and formed the crack source at the phase boundary during the tensile process, which caused the alloy fracture and significantly reduced the plasticity and strength.

3.3 Dislocations and precipitated phases

Figure 7 shows the dislocation morphology of the AQ piece and the TSR piece. As shown in Figure 7a, copious dislocation lines appeared and some dislocation lines were tangled massively into spirals, especially with fine

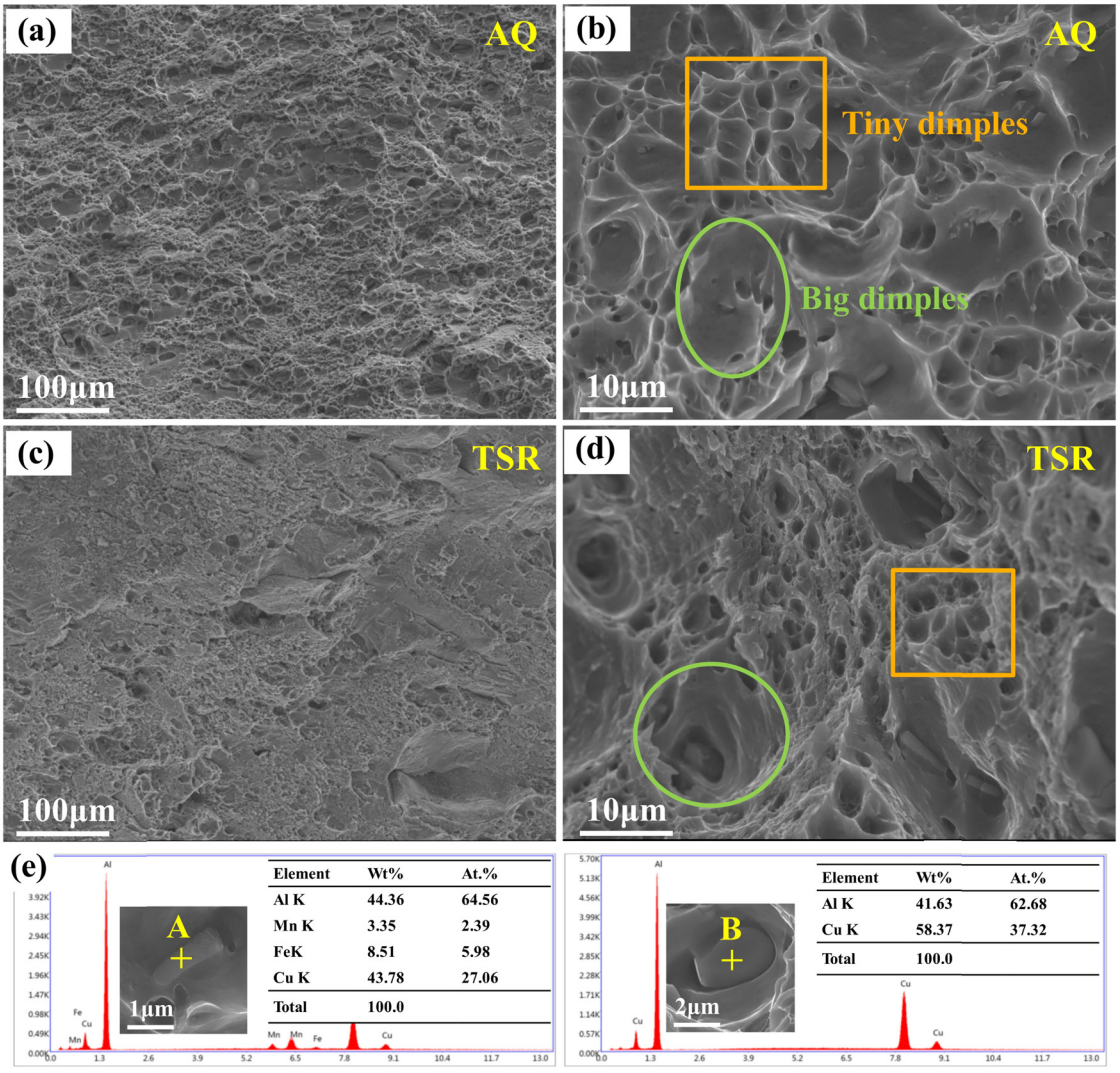

Figure 6: SEM images of tension-fracture surfaces: (a and b) AQ piece, (c and d) TSR piece, and (e) EDS analysis of particles.

particles with an average size of 0.2 μm. These particles were confirmed as θ-phase (Al_2Cu particles) in Al–Cu alloys by EDS analysis [37]. Further, the dislocation distribution was inhomogeneous, and dislocation-free and dislocation-tangled areas coexisted. In contrast, the number of dislocations of TSR was noticeably smaller (Figure 7b), and only a few dislocation lines were distributed randomly, small and vaguely visible, which were severely trapped by the precipitated phases. Additionally, dislocations can only be rarely observed between precipitated phases. This suggests the immovable nature of the dislocations in the TSR piece.

Figure 8 shows TEM and STEM images and the corresponding selected area electron diffraction (SAED) pattern of the AQ piece and the TSR piece obtained near the $[001]_{Al}$ zone axis. Figure 8a shows that the matrices of the AQ piece were very pure without any precipitated phases after solution treatment, indicating that the alloy was still in the supersaturated solid solution phase. The TSR piece (Figures 8b1 and b2) showed a high number density of precipitated phases, with the length of the precipitates ranging from 120 to 480 nm and a thickness of approximately 2–6 nm. The corresponding SAED pattern clearly displays an obvious increase in the streak intensity at the $\{110\}_{Al}$ positions, confirming the presence of a high fraction of θ′ phase precipitates in this sample. The presence of θ′ phases was further confirmed by the high-resolution TEM micrograph shown in Figure 8b3. The distribution of these θ′ phases was uniform but accompanied by preferential orientation precipitation, that is, stress orientation effect (SOE).

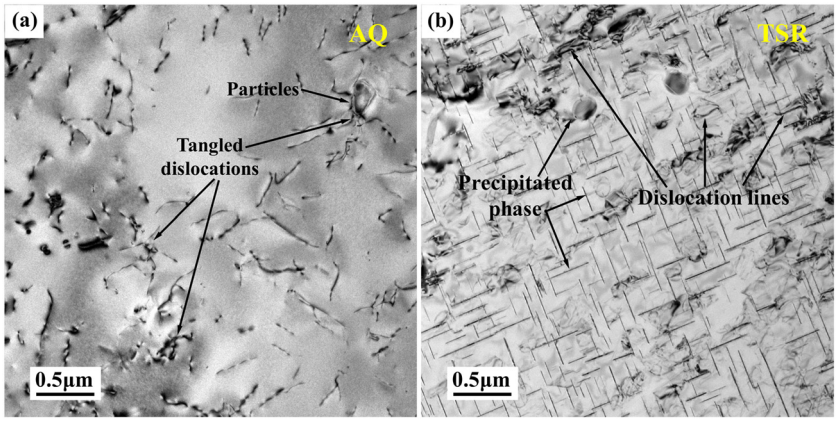

Figure 7: TEM images of dislocation characteristics: (a) AQ piece and (b) TSR piece.

3.4 Grain structures and second phase particles

Figure 9 shows the OM microstructures of the AQ piece and the TSR piece. There was little variation in the grain size between the AQ piece (Figure 9a) and the TSR piece (Figure 9b), the grains were coarse and elongated along the CD, and a large number of coarse Al_2Cu particles still existed in the matrix. These coarse second-phase Al_2Cu particles appear because the mass fraction of Cu in 2219 Al–Cu alloys ranges from 5.8 to 6.8% and exceeds the solubility limit of Cu in the Al matrix (5.65%) [2]. Therefore, the size and shape of the grains and the coarse Al_2Cu particles were not obviously changed by TSR at a temperature below the recrystallization temperature, indicating that TSR can only cause the micro-plastic

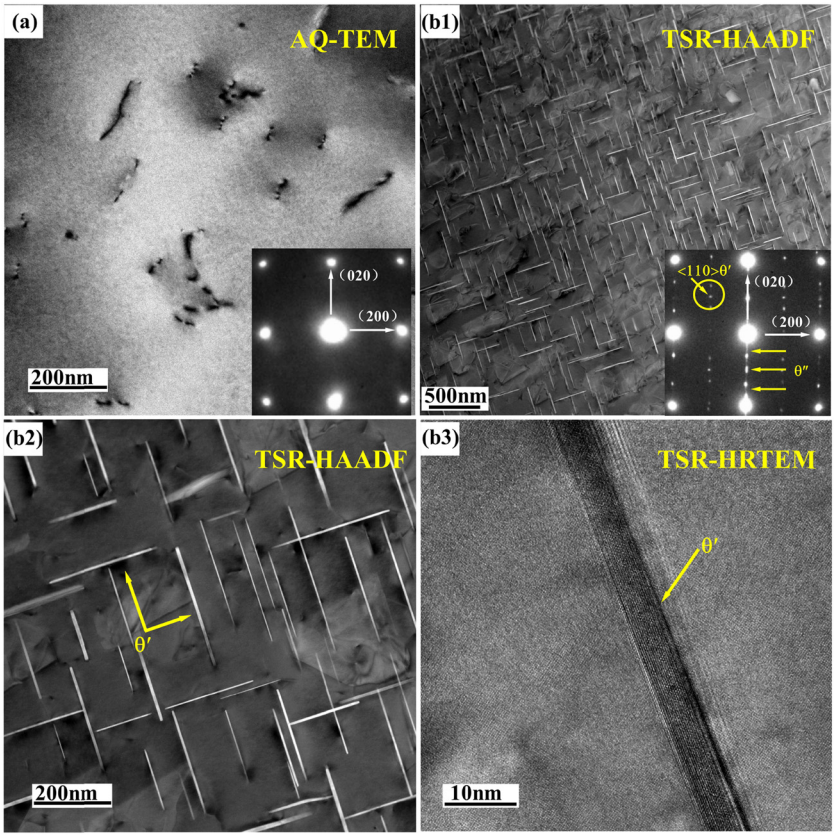

Figure 8: TEM/STEM images and corresponding SAED patterns of precipitated phase characteristics: (a) AQ piece and (b1–b3) TSR piece.

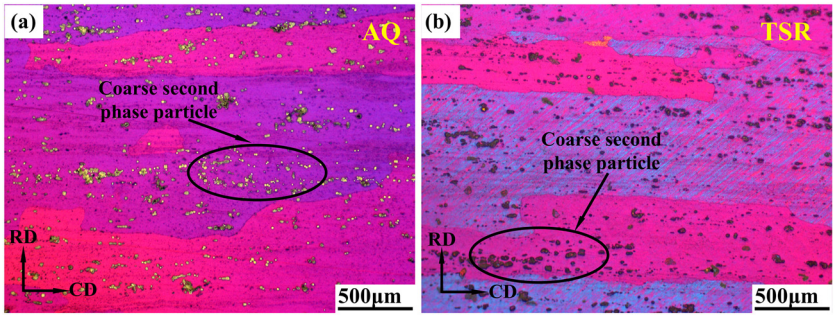

Figure 9: OM images of grain structures and coarse second-phase particles: (a) AQ piece and (b) TSR piece.

deformation within the grain interior, but not the macroplastic deformation.

4 Discussion

4.1 Evolution and relief mechanism of residual stress during TSR

In general, in the quenching process of large Al alloy rings, the residual elastic deformation caused by the uneven temperature of each part of the workpiece is the main reason for the internal residual stress. As shown in Figure 10a, the residual stress relief in the TSR process is the result of the transformation of residual elastic strain into inelastic strain. The total strain remains unchanged because there is no new deformation in the workpiece, and the strain relationship can be expressed as follows [38,39]:

$$\varepsilon_{tot} = \varepsilon_e + \varepsilon_{pl} + \varepsilon_c = \varepsilon_e + \varepsilon_{ie}, \tag{1}$$

$$\dot{\varepsilon}_e = -\dot{\varepsilon}_{ie} = -\frac{d\sigma}{E \cdot dt}, \tag{2}$$

where ε_{tot}, ε_e, ε_{pl}, ε_c, and ε_{ie} are the total strain, elastic strain, plastic strain, creep strain, and inelastic strain, respectively; $\dot{\varepsilon}_e$ and $\dot{\varepsilon}_{ie}$ are the elastic and inelastic strain rates, respectively. $\dot{\varepsilon}_{ie}$ is the derivative of residual stress σ divided by the elastic modulus E over time t.

The inelastic strain (including plastic strain, creep strain, etc.) of metals is caused by the motion and multiplication of dislocations. Dislocations are micro defects in the crystal materials, which are the local dislocation of atoms and belong to the line defects from the geometric point of view. Under the action of external force, dislocations slide along a specific direction in the slip plane, which eventually lead to the generation of inelastic strain [39]. The inelastic strain rates $\dot{\varepsilon}_{ie}$ can be calculated by the Orowan equation [40,41]:

$$\dot{\varepsilon}_{ie} = \rho_m \bar{v} b / M, \tag{3}$$

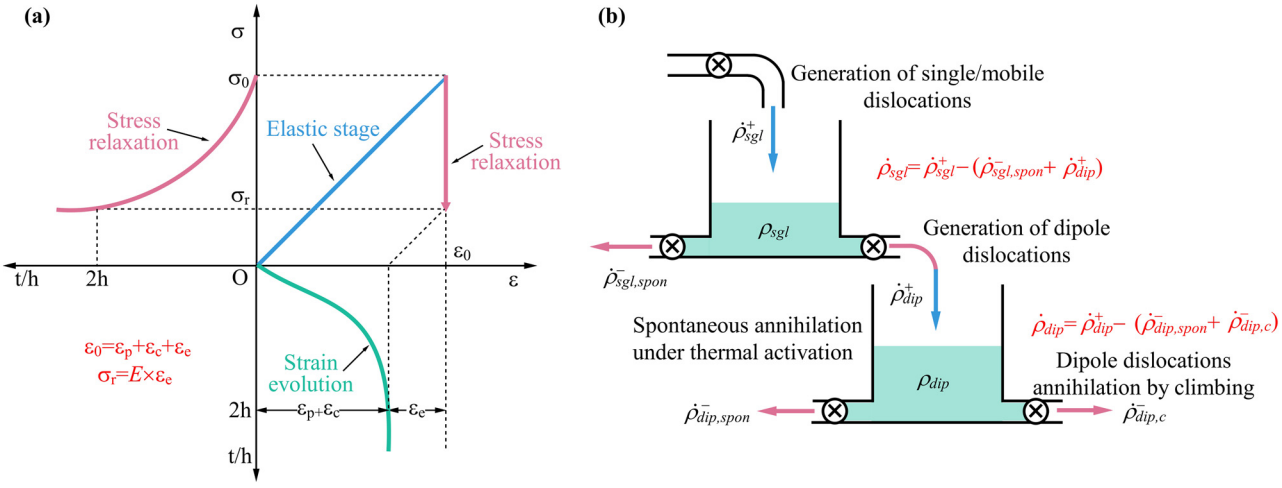

Figure 10: Schematic illustration of residual stress relief mechanisms in the TSR process: (a) corresponding relationship between stress and strain in the process of TSR and (b) evolution of dislocation density.

where ρ_m is the density of the mobile dislocations in the material, $\bar{v}$ is the average velocity of dislocations, b is the mode of the Burgers vector (=0.286 nm for Al) [42], and M is the Taylor factor of face-centered cubic crystal (=3.06 for Al) [42].

Therefore, in order to study the inelastic strain and inelastic strain rate, and then establish a residual stress relief model, it is necessary to analyze the evolution behavior of dislocation density during TSR. Dislocations are the carrier of inelastic deformation, and inelastic strain is caused by the motion, multiplication, annihilation, and transformation of dislocations, i.e., dynamic evolution behavior of dislocations. As shown in Figure 10b, the evolution rate of the total dislocation density is the sum of the single dislocation density and dipole dislocation density according to the dislocation evolution theory proposed by Blum et al. [40,43,44]:

$$\rho = \rho_{sgl} + \rho_{dip}, \tag{4}$$

$$\dot{\rho} = \dot{\rho}_{sgl} + \dot{\rho}_{dip}, \tag{5}$$

where ρ, ρ_{sgl}, and ρ_{dip} are total dislocation density, single dislocation density, and dipole dislocation density, respectively. A single dislocation is a mobile dislocation; that is, $\rho_m = \rho_{sgl}$. The single dislocation density can be expressed as follows:

$$\begin{aligned}\dot{\rho}_{sgl} &= \dot{\rho}^{+}_{sgl} - (\dot{\rho}^{-}_{sgl,spon} + \dot{\rho}^{+}_{dip}) \\ &= \frac{\dot{\varepsilon}_{ie}}{K_\Lambda b}\sqrt{\rho} - \frac{M}{b}\dot{\varepsilon}_{ie} \times 2d_{dip} \times \frac{2\rho_{sgl}}{n_g},\end{aligned} \tag{6}$$

and the dipole dislocations in plastic deformation can be described as follows:

$$\begin{aligned}\dot{\rho}_{dip} &= \dot{\rho}^{+}_{dip} - (\dot{\rho}^{-}_{dip,spon} + \dot{\rho}^{-}_{dip,c}) \\ &= \left(\left(1 - \frac{6b}{d_{dip}}\right)\rho_{sgl} - \rho_{dip}\right) \\ &\quad \times \frac{M}{b}\dot{\varepsilon}_{ie} \times 4d_{dip} - \rho_{dip} \times \frac{4v_c}{d_{dip} - 6b},\end{aligned} \tag{7}$$

where $\dot{\rho}^{+}_{sgl}$ is the accumulation rate of single dislocations, $\dot{\rho}^{-}_{sgl,spon}$ is the spontaneous annihilation rate of single dislocations, $\dot{\rho}^{+}_{dip}$ is the accumulation rate of dipole dislocations, $\dot{\rho}^{-}_{dip,spon}$ is the spontaneous annihilation rate of dipole dislocations, and $\dot{\rho}^{-}_{dip,c}$ is the thermal activation annihilation rate of dipole dislocations. K_Λ is a dimensionless constant related to the material, d_{dip} is the shortest distance to form a dipole dislocation, n_g is the number of active slip systems, and v_c is the climbing velocity of dislocation motion.

Residual stresses originate from the elastic accommodation of misfits between different regions in a structure [45]. It can be considered that the residual stress is the elastic stress in an equilibrium state, which is the mutual restraint between the plastic deformation part and the non-plastic deformation part. The essence of the residual stress is lattice distortion, which is largely caused by dislocations. Therefore, there are two ways to relieve the residual stress: (1) give the metal atom enough energy to intensify the vibration and return to the equilibrium position, so as to reduce the lattice distortion; (2) make those parts in the elastic stress state achieve the plastic yield, so as to reduce the elastic stress of the metal, and then achieve the purpose of reducing the residual stress [46].

Based on the above analysis of the residual stress in the process of TSR, the mechanism of TSR on residual stress relief can be summarized from the macroscopic and microscopic perspectives. From the macroscopic perspective, the yield stress and elastic modulus of metal materials decrease with the increase in heating temperature. When the yield stress is lower than the residual stress, the plastic yield will occur in the workpiece, thus releasing the elastic stress and reducing the residual stress. Since the grain size and shape had no significant change after TSR (Figure 9), it is almost impossible to achieve the macro-plastic yield, but the stress relief effect can still be produced in the process of TSR (Figure 3). This phenomenon can be explained that micro-plastic deformation has occurred in the elastic range of the material before the yield of the material as a whole, and the micro-plastic deformation only occurs inside some grains of the material. Considering the combined action of residual stress and temperature, a variety of creep mechanisms may be activated, which will cause a large relief of internal residual stress.

From the microscopic perspective, the dislocations in the stress concentration region are activated due to the input of thermal energy, and the dislocations slip along the slip plane and small inelastic strains (plastic deformation, creep, etc.) appear. There is no sufficient energy to break through the grain boundary constraints, so the dislocations inside the grains are not enough to excite the dislocation sources of adjacent grains, and the micro-plastic deformation produced by the dislocations is not enough to change the grain shape and size. In the process of dislocation motion, dislocation proliferation, stacking, and entanglement occur constantly, the mobile dislocations become immobile dislocations (i.e., pinned) or disappear and the dislocation configuration is more stable (Figure 7). Therefore, the lattice distortion decreases, the lattice arrangement tends to balance, and the residual stress decreases. With the extension of stress relief time, the motion resistance becomes larger due to the continuous

increase in the precipitated phases. When the motion resistance is balanced with the residual stress, the motion stops, and the TSR treatment process is completed.

4.2 Strengthening mechanisms of mechanical properties during TSR

The strengthening effect of 2219 Al–Cu alloy comes from many aspects, and the change in macro strength is usually the result of the comprehensive action of various strengthening mechanisms. These mechanisms mainly involve four types of strengthening: dislocation, fine-grain, solid-solution, and precipitation strengthening. The contribution of various strengthening mechanisms to strength can be expressed as follows [37,42]:

$$\sigma_y = \sigma_0 + \sigma_{gb} + \sigma_{ss} + \sqrt{\sigma_{dis}^2 + \sigma_{ppt}^2}, \tag{8}$$

$$\sigma_{gb} = \frac{k}{\sqrt{d}}, \tag{9}$$

$$\sigma_{ss} = M\sum H_i \cdot C_i^{2/3}, \tag{10}$$

$$\sigma_{dis} = M\alpha Gb\sqrt{\rho}, \tag{11}$$

$$\sigma_{ppt} = 0.13MG\frac{b}{2\sqrt{rh}}\left[f_v^{1/2} + 0.75\left(\frac{r}{h}\right)^{1/2} f_v + 0.14\left(\frac{r}{h}\right) f_v^{3/2}\right]\ln\left(\frac{0.158r}{r_0}\right), \tag{12}$$

where σ_0 denotes the lattice friction stress, σ_{gb}, σ_{ss}, σ_{dis}, and σ_{ppt} represent the strengths contributed by grain boundary strengthening, solid-solution strengthening, dislocation strengthening, and precipitation strengthening, respectively; k is an experimental constant, d is the average grain diameter, H_i is a constant related to the properties of the related solute i, C_i is the solute concentration, α is an average value of the junctions strength over all existing configurations [47], G is the shear modulus, r_0 is the inner radius of dislocations around strengthening phases, r, h, and f_v are the radius, thickness, and volume fraction of θ′ phases, respectively.

The experimental results showed that the strength of the TSR piece was higher than that of the AQ piece, and the changing trend of hardness was basically consistent with that of strength (Figure 5). The sketch in Figure 11a summarizes the microstructure evolution of 2219 Al–Cu alloy during TSR at 175°C for 2 h. The grain size had no obvious change by metallographic observation (Figure 9), which indicates that the grain boundary strengthening was not the main strengthening mode. The experimental results showed that the number of precipitated phases increased (Figure 8), and that the dislocation density decreased (Figure 7). The solute atoms (Cu) precipitate from the Al matrix, and the solid solution concentration decreases significantly with more precipitated phases. The shadow in Figure 11a represents the solid solution concentration. The deeper the shadow, the greater the solid solution concentration. From equation (8), it can be seen that the contribution to strength is positively correlated with the number of precipitated phases, dislocation density, and the solid solubility, while only the number of precipitated phases was consistent with the changing trend of strength. Thus, precipitation strengthening was the main strengthening mechanism of 2219 Al–Cu alloy during TSR. Equation (12) shows that the increase in strength caused

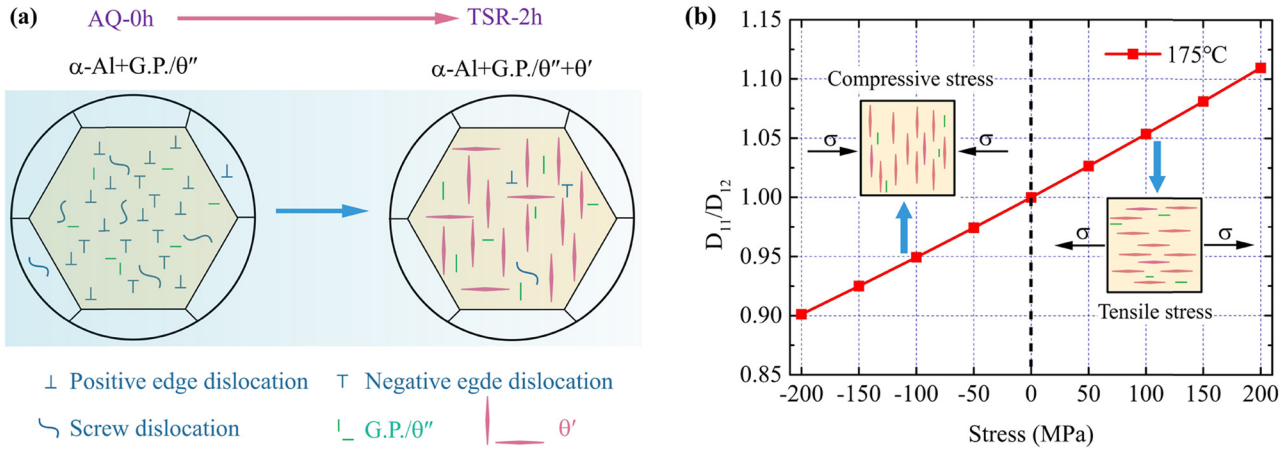

Figure 11: Schematic illustration of strengthening mechanisms of 2219 alloy during TSR at 175°C for 2 h: (a) microstructural evolution, and (b) diffusion coefficient ratio along two different directions under stress. The shadow represents the solid solution concentration.

by the θ′ phase is clearly associated with its size (radius and thickness) and volume fraction. Therefore, the TSR piece with a higher density of θ′ phases obtains a higher strength.

The precipitation sequence of the precipitated phases in 2219 Al–Cu alloy is: supersaturated solid solution → Guinier–Preston (G.P.) zones → coherent θ″ (Al_3Cu) → semi-coherent θ′ (Al_2Cu) → stable θ (Al_2Cu) [47]. The precipitated phases have different habitual surfaces, θ′ phase mainly precipitates at $\{100\}_{Al}$ planes. From the perspective of precipitation kinetics, the precipitation of precipitated phases needs to overcome a certain energy barrier in the initial nucleation stage. Temperature as energy inputs is an important factor for promoting nucleation of precipitated phases during TSR. The nucleation rate can be calculated by classical nucleation theory [48,49]:

$$\left.\frac{\mathrm{d}f_v}{\mathrm{d}t}\right|_{\text{nucleation}} = A_0 N_0 Z\beta\star \exp\left(-\frac{\Delta G^*}{k_\beta T}\right)\exp\left(-\frac{\tau}{t}\right), \quad (13)$$

$$\beta^* = \frac{\left[2\pi(r_p^*)^2 + \frac{4\pi(r_p^*)^2}{A}\right]DC_0}{a^4}, \quad (14)$$

$$\tau = \frac{1}{2\beta^* Z}, \quad (15)$$

where A_0 is the Avogadro constant, N_0 is the number of atoms per unit volume, Z is the Zeldovich non-equilibrium factor (≈1/20) [50], k_β is the Boltzmann constant, T is the heating temperature of TSR, τ is the incubation time, t is the heating time of TSR, r_p^* is the critical nucleation radius of precipitated phases, D is the diffusion rate of solute atoms in the solvent, C_0 is the concentration of solute in the parent phase, A is the ratio of the length to the diameter of precipitated phases, a is the lattice constant of precipitated phases, and ΔG^* is the variation in the critical nucleation free energy including the influence of dislocations and other nucleation factors. The precipitated phases can preferentially nucleate and grow near the dislocation defects, grain boundary, or phase boundary with high free energy. Therefore, equation (13) is in fact quasi-uniform nucleation, which is the assumption that the precipitated phases are uniformly distributed and precipitated under non-uniform nucleation conditions.

Under the action of residual stress introduced by quenching, the precipitation behavior of the θ′ phase changes in all directions and is easier to precipitate on the $[100]_{Al}$ plane parallel to the stress axis, that is, the precipitation of θ′ phase has SOE. According to the theory of atomic migration dynamics, the SOE of θ′ phases in the process of TSR can be explained by the diffusion mechanism. The diffusion coefficient ratio in two different directions (perpendicular to each other) under the action of stress is as follows [51,52]:

$$\frac{D_{11}}{D_{12}} \approx \left(\frac{12KC - 2\sigma C_{12}}{12KC + \sigma C_{11}}\right)^2 \cdot\exp[15\sigma(C_{11} + 2C_{12})Q_M/(36KCRT)], \quad (16)$$

$$K = (C_{11} + 2C_{12})/2, \quad (17)$$

$$C = (C_{11} + C_{12})/3, \quad (18)$$

where σ is the stress; C_{11} and C_{12} are the elastic stiffness constants, $C_{11} = 1.082 \times 10^5$ MPa and $C_{12} = 6.13 \times 10^4$ MPa [53]; Q_M is the diffusion activation energy of vacancy, $Q_M = 1.3 \times 10^5$ J·mol^{-1}; and R is the gas constant, R =8.314 J·(mol·K)$^{-1}$. The heating temperature T = 448 K. As shown in Figure 11b, the change in diffusion coefficient ratio of Al alloy along two different directions under stress at 175°C is obtained according to equation (16).

It can be seen from Figure 11b that under the condition of no stress, the diffusion coefficient ratio along two different directions is $D_{11}/D_{12} = 1$, which indicates that the diffusion coefficient is isotropic. If the applied stress is compressive stress, the diffusion coefficient ratio along two different directions is $D_{11}/D_{12} < 1$, and the precipitated phase will preferentially precipitate along the direction perpendicular to the stress. If the applied stress is tensile stress, the ratio of diffusion coefficients along two different directions is $D_{11}/D_{12} > 1$, and the precipitated phase will preferentially precipitate along the direction parallel to the stress. These analyses indicate that the stress makes the difference in diffusion coefficients along two different directions. The higher the applied stress level (i.e., the greater the absolute value of stress), the more the diffusion coefficient ratio deviates from 1. That means the greater the difference between the two directions, and the diffusion coefficient shows obvious anisotropy, indicates that the applied stress can produce the SOE by changing the precipitation velocity of the precipitated phases along different directions. As shown in Figure 3, the average initial stresses along the two directions are −116.11 and −87.35 MPa. When the temperature is 175°C, under the combined action of compressive stress along both directions, the precipitated phases in the alloy produce obvious SOE (Figures 8 and 11a). Therefore, the applied stress will make the precipitated phases in the alloy preferentially precipitate along the tensile stress direction, which will significantly improve the mechanical properties of the alloy along this direction, but the mechanical properties perpendicular to the tensile stress direction may be weakened.

To address the problem of shortage of stress relief equipment for large rings, ref. [39] has made more

Table 2: Comparison of experimental results between TSR and STVSR [39]

Experimental results	STVSR (Optimal position O)	TSR
Stress relief rate (CD and AD)	44.43 and 45.14%	86.37 and 85.77%
Increment in UTS, YS, and $HV_{0.1}$	67 MPa, 53 MPa, and 19 $HV_{0.1}$	85.98 MPa, 98.46 MPa, and 27.8 $HV_{0.1}$
Fracture morphology	More and deeper dimples	Fewer and shallower dimples
Dislocation	Higher density	Lower density
Precipitated phase	G.P. zones and θ″ phases	G.P. zones, θ″ and θ′ phases
Grain and second-phase particle	Almost unchanged	Almost unchanged

consideration on economy and portability, and carried out stress relief treatment for rings section by section. Considering that there is a large temperature gradient at the junction between the heating zone and the non-heating zone on both sides of the furnace, the superposition of TSR and vibration stress relief (VSR) is introduced into the large rings to compensate for heat loss, that is, the so-called segmented thermal-vibration stress relief (STVSR). However, the research on TSR in this study belongs to general basic scientific research, which can be applied to large and small-size rings or other components, suggesting that the application object and application scope are wider. Accordingly, its underlying mechanisms are more general and universal. Remarkably, the comparison of experimental results between TSR and STVSR (Table 2) indicates that the stress relief and strengthening effect of TSR are superior to those of STVSR at the same temperature (175°C).

The actual temperature in the furnace of TSR with better air tightness is higher and more uniform than that of STVSR, thus an excellent comprehensive effect can still be achieved without the superposition of VSR. The findings confirm that temperature plays a dominant role in stress relaxation. In an appropriate range, with the increase in temperature, the dislocation motion is more intense and the dislocation recovery is more sufficient, resulting in a more stable configuration. Meanwhile, the driving force of precipitation is greatly improved, and then the density of precipitated phases (semi-coherent θ′ phases) with greater strengthening effect is higher. Under the interaction of dislocations and precipitated phases, TSR in the present work produces a higher stress reduction rate and better aging strengthening effect than STVSR in ref. [39], which can better achieve the purpose of synergistic optimization of residual stress and mechanical properties.

Since the underlying mechanisms of stress relief and strengthening effects during TSR are established based on the microscopic interaction between dislocations and precipitated phases, it is anticipated that they can be applied to describe the stress relief mechanisms of other heat-treatable aluminum alloys, e.g., other 2xxx and even 6xxx and 7xxx series Al alloys. However, necessary modifications have to be made to fully account for the difference in dislocation mobility in different alloy systems and the varying strengthening mechanisms with various types of precipitated phases.

5 Conclusion

The effects of the TSR treatment method on the residual stresses, microstructures, and mechanical properties of the large 2219 Al–Cu alloy transition ring were studied. The underlying mechanisms of effects of TSR on these aspects were then analyzed. Based on the results obtained, the following conclusions can be drawn:

(1) The circumferential and axial stress relief rates of the test piece treated by TSR can reach 86.37 and 85.77%, respectively, and the maximum and minimum principal stress relief rates of the test piece treated by TSR can reach 91.58 and 83.04%, respectively. The maximum range and maximum average standard deviation decreased from 103.74 and 30.25 MPa to 17.23 and 8.00 MPa, respectively. These results show that TSR has a desirable effect on relieving and homogenizing residual stress.
(2) The UTS, YS, and $HV_{0.1}$ of the TSR piece were higher than those of the AQ piece, increased by 85.98 MPa, 98.46 MPa, and 27.8 $HV_{0.1}$, respectively. However, the EL of the TSR piece was lower than that of the AQ piece with a decrease by 13.38%. The main fracture mode of the two pieces was microporous aggregation ductile fracture.
(3) The AQ piece showed copious dislocations with no distinct precipitated phases, but TSR showed a noticeably smaller number of dislocations with a higher density of uniformly distributed θ′ phases. The size and shape of the grains and the coarse Al_2Cu particles were not obviously changed by TSR, which indicates that

TSR can only cause micro-plastic deformation within the grain interior, but not macro-plastic deformation.

(4) The evolution process of dislocation density in the process of TSR includes dislocation accumulation and annihilation, in which the dislocation annihilation process is dominant. This reduces the dislocation density, changes the dislocation configuration, and reduces the lattice distortion, which relaxes the residual stress in the material. Therefore, the residual stress relief is attributed to the dynamic evolution behavior of dislocations during TSR.

(5) Precipitation strengthening was the main strengthening mechanism of 2219 Al–Cu alloy treated by TSR. The heterogeneous nucleation of θ′ phases was induced by dislocation motion. The θ′ phases have a preferred orientation distribution (i.e., SOE) due to the high residual stress introduced by quenching, which weakened the strength of the alloy to a certain extent.

Funding information: The work is financially supported by the National Natural Science Foundation of China [grant number 52005018 and 51875024], the Aeronautical Science Foundation of China [grant number 2019ZE051002], the National Defense Basic Scientific Research Program of China [JCKY2018601C002], and the China Academy of Launch Vehicle Technology Foundation [CALT2021-23]. The authors gratefully acknowledge these supports.

Author contributions: Four authors have made irreplaceable work on this paper. Hechuan Song: conceptualization, methodology, investigation, and Writing – original draft. Hanjun Gao: conceptualization, validation, writing – review and editing, and funding acquisition. Qiong Wu: validation, formal analysis, visualization, funding acquisition. Yidu Zhang: Resources, supervision, data curation, and funding acquisition. All authors have discussed and agreed to the published version of the manuscript.

Conflict of interest: Authors state no conflict of interest.

Data availability statement: The raw data related to this manuscript will be made available on request.

References

[1] Wu, Q., J. Wu, Y. D. Zhang, H. J. Gao, and H. David. Analysis and homogenization of residual stress in aerospace ring rolling process of 2219 aluminum alloy using thermal stress relief method. *International Journal of Mechanical Sciences*, Vol. 157–158, 2019, pp. 111–118.

[2] He, H. L., Y. P. Yi, S. Q. Huang, and Y. X. Zhang. Effects of deformation temperature on second-phase particles and mechanical properties of 2219 Al–Cu alloy. *Materials Science and Engineering A*, Vol. 712, 2018, pp. 414–423.

[3] Gong, H., X. L. Sun, Y. Q. Liu, Y. X. Wu, Y. N. Wang, and Y. J. Sun. Residual stress relief in 2219 aluminum alloy ring using roll-bending. *Materials*, Vol. 13, No. 1, 2019, id. 105.

[4] Wang, L., X. Chen, T. Luo, H. Ni, L. Mei, P. Ren, et al. Effect of cross cold rolling and annealing on microstructure and texture in pure nickel. *Reviews on Advanced Materials Science*, Vol. 59, No. 1, 2020, pp. 252–263.

[5] Xu, Y. S., J. Zhong, B. H. Li, and Z. Zhang. Effects of TVSR process on the dimensional stability and residual stress of 7075 aluminum alloy parts. *Reviews on Advanced Materials Science*, Vol. 60, No. 1, 2021, pp. 631–642.

[6] Shen, H. S., Y. Xiang, and Y. Fan. Large amplitude vibration of doubly curved FG-GRC laminated panels in thermal environments. *Nanotechnology Reviews*, Vol. 8, No. 1, 2019, pp. 467–483.

[7] Li, B., S. F. Wu, and X. S. Gao. Theoretical calculation of a Tio2-tased photocatalyst in the field of water splitting: A review. *Nanotechnology Reviews*, Vol. 9, No. 1, 2020, pp. 1080–1103.

[8] Song, H. C., Y. D. Zhang, Q. Wu, and H. J. Gao. Low-stiffness spring element constraint boundary condition method for machining deformation simulation. *Journal of Mechanical Science and Technology*, Vol. 34, No. 10, 2020, pp. 4117–4128.

[9] Jung, C. Y. and J. H. Lee. Crack closure and flexural tensile capacity with SMA fibers randomly embedded on tensile side of mortar beams. *Nanotechnology Reviews*, Vol. 9, No. 1, 2020, pp. 354–366.

[10] Yu, H., L. Zhang, F. Cai, S. Zhong, J. Ma, L. Bao, et al. Microstructure and mechanical properties of brazing joint of silver-based composite filler metal. *Nanotechnology Reviews*, Vol. 9, No. 1, 2020, pp. 1034–1043.

[11] Lee, S. Y. and J. G. Hwang. Finite element nonlinear transient modelling of carbon nanotubes reinforced fiber/polymer composite spherical shells with a cutout. *Nanotechnology Reviews*, Vol. 8, No. 1, 2019, pp. 444–451.

[12] Vardanjani, M. J., M. Ghayour, and R. M. Homami. Analysis of the vibrational stress relief for reducing the residual stresses caused by machining. *Experimental Techniques*, Vol. 40, No. 2, 2016, pp. 705–713.

[13] Mohanty, S., M. Arivarasu, N. Arivazhagan, and K. V. Phani Prabhakar. The residual stress distribution of CO_2 laser beam welded AISI 316 austenitic stainless steel and the effect of vibratory stress relief. *Materials Science and Engineering A*, Vol. 703, 2017, pp. 227–235.

[14] Ran, P., T. Pirling, J. Zheng, J. Lin, and C. M. Davies. Quantification of thermal residual stresses relaxation in AA7xxx aluminium alloy through cold rolling. *Journal of Materials Processing Technology*, Vol. 264, 2018, pp. 454–468.

[15] Bruno, G., R. Fernández, and G. González-Doncel. Relaxation of the residual stress in 6061Al-15 vol% SiC_w composites by isothermal annealing. *Materials Science & Engineering A*, Vol. 382, No. 1–2, 2004, pp. 188–197.

[16] Epp, J., H. Surm, T. Hirsch, and F. Hoffmann. Residual stress relaxation during heating of bearing rings produced in two

different manufacturing chains. *Journal of Materials Processing Technology*, Vol. 211, No. 4, 2011, pp. 637–643.
[17] Kim, J. S., J. H. Yoo, and Y. J. Oh. A study on residual stress mitigation of the HDPE pipe for various annealing conditions. *Journal of Mechanical Science and Technology*, Vol. 29, No. 3, 2015, pp. 1065–1073.
[18] Younger, M. S. and K. H. Eckelmeyer. *Overcoming residual stresses and machining distortion in the production of aluminum alloy satellite boxes. Sandia report SAND2007-6811*, Sandia National Laboratories, Albuquerque, NM, 2007.
[19] Xie, L. C., C. H. Jiang, and V. Ji. Thermal relaxation of residual stress in shot peened surface layer of (TiB + TiC)/Ti-6Al-4V composite at elevated temperatures. *Materials Science and Engineering A*, Vol. 528, No. 21, 2011, pp. 6478–6483.
[20] Madariaga, A., J. Aperribay, P. J. Arrazola, J. A. Esnaola, E. Hormaetxe, A. Garay, et al. Effect of thermal annealing on machining-induced residual stresses in Inconel 718. *Journal of Materials Engineering and Performance*, Vol. 26, 2017, pp. 3728–3738.
[21] Ren, X. D., W. F. Zhou, S. D. Xu, S. Q. Yuan, N. F. Ren, Y. Wang, et al. Iron GH2036 alloy residual stress thermal relaxation behavior in laser shock processing. *Optics & Laser Technology*, Vol. 74, 2015, pp. 29–35.
[22] Shalvandi, M., Y. Hojjat, A. Abdullah, and H. Asadi. Influence of ultrasonic stress relief on stainless steel 316 specimens: a comparison with thermal stress relief. *Materials & Design*, Vol. 46, 2013, pp. 713–723.
[23] Fu, P. and C. H. Jiang. Residual stress relaxation and microstructural development of the surface layer of 18CrNiMo7 steel after shot peening during isothermal annealing. *Materials & Design*, Vol. 56, 2014, pp. 1034–1038.
[24] Zhang, Y., X. Jiang, H. Sun, and Z. Shao. Effect of annealing heat treatment on microstructure and mechanical properties of nonequiatomic CoCrFeNiMo medium-entropy alloys prepared by hot isostatic pressing. *Nanotechnology Reviews*, Vol. 9, No. 1, 2020, pp. 580–595.
[25] Lin, N., R. Xie, J. Zou, J. Qin, Y. Wang, S. Yuan, et al. Surface damage mitigation of titanium and its alloys via thermal oxidation: A brief review. *Reviews on Advanced Materials Science*, Vol. 58, No. 1, 2019, pp. 132–146.
[26] Dong, Y. B., W. Z. Shao, J. T. Jiang, and B. Y. Zhang. Minimization of residual stress in an Al–Cu alloy forged plate by different heat treatments. *Journal of Materials Engineering and Performance*, Vol. 24, No. 6, 2015, pp. 2256–2265.
[27] Pan, L., W. He, and B. P. Gu. Non-uniform carbon segregation induced by electric current pulse under residual stresses. *Journal of Materials Processing Technology*, Vol. 226, 2015, pp. 247–254.
[28] Pan, L., W. He, and B. P. Gu. Effects of electric current pulses on mechanical properties and microstructures of as-quenched medium carbon steel. *Materials Science and Engineering A*, Vol. 662, 2016, pp. 404–411.
[29] Xiang, S. Q. and X. F. Zhang. Residual stress removal under pulsed electric current. *Acta Metallurgica Sinica* (*English Letters*), Vol. 33, No. 2, 2020, pp. 281–289.
[30] Quan, S., J. Kang, Z. Xing, H. Wang, Y. F. Huang, G. H. Ma, et al. Effect of pulsed magnetic field treatment on the residual stress of 20Cr2Ni4A steel. *Journal of Magnetism and Magnetic Materials*, Vol. 476, 2019, pp. 218–224.
[31] Huang, G., Q. D. Zhang, B. Y. Zhang, and S. Li. Microscopic mechanism of the combined magnetic-vibration treatment for residual stress reduction. *Results in Physics*, Vol. 29, 2021, id. 104659.
[32] Cai, Z. P. and X. Q. Huang. Residual stress reduction by combined treatment of pulsed magnetic field and pulsed current. *Materials Science and Engineering A*, Vol. 528, 2011, pp. 6287–6292.
[33] Yang, J., J. X. Dong, H. Jiang, and Z. H. Yao. "Λ"-shaped trend of stress relaxation stability of Inconel718 superalloy with initial stress increasing. *Materialia*, Vol. 9, 2019, id. 100570.
[34] Muhamad, S. S., J. A. Ghani, C. H. C. Haron, and H. Yazid. Cryogenic milling and formation of nanostructured machined surface of AISI 4340. *Nanotechnology Reviews*, Vol. 9, No. 1, 2020, pp. 1104–1117.
[35] Selim, M. M. and S. A. El-Safty. Vibrational analysis of an irregular single-walled carbon nanotube incorporating initial stress effects. *Nanotechnology Reviews*, Vol. 9, No. 1, 2020, pp. 1481–1490.
[36] Steinzig, M., D. Upshaw, and J. Rasty. Influence of drilling parameters on the accuracy of hole-drilling residual stress measurements. *Experimental Mechanics*, Vol. 54, 2014, pp. 1537–1543.
[37] He, H. L., Y. P. Yi, S. Q. Huang, and Y. X. Zhang. An improved process for grain refinement of large 2219 Al alloy rings and its influence on mechanical properties. *Journal of Materials Science and Technology*, Vol. 35, 2019, pp. 55–63.
[38] Rahimi, S., M. King, and C. Dumont. Stress relaxation behaviour in IN718 nickel-based super alloy during ageing heat treatments. *Materials Science and Engineering A*, Vol. 708, 2017, pp. 563–573.
[39] Song, H. C., H. J. Gao, Q. Wu, and Y. D. Zhang. Effects of segmented thermal-vibration stress relief process on residual stresses, mechanical properties and microstructures of large 2219 Al alloy rings. *Journal of Alloys and Compounds*, Vol. 886, 2021, id. 161269.
[40] Blum, W., P. Eisenlohr, and F. Breutinger. Understanding creep – a review. *Metallurgical and Materials Transactions A*, Vol. 33, No. 2, 2002, pp. 291–303.
[41] Antolovich, S. D. and R. W. Armstrong. Plastic strain localization in metals: origins and consequences. *Progress in Materials Science*, Vol. 59, 2014, pp. 1–160.
[42] Lan, J., X. Shen, J. Liu, and L. Hua. Strengthening mechanisms of 2A14 aluminum alloy with cold deformation prior to artificial aging. *Materials Science and Engineering A*, Vol. 745, 2019, pp. 517–535.
[43] Blum, W. and P. Eisenlohr. Dislocation mechanics of creep. *Materials Science and Engineering A*, Vol. 510, No. 10, 2015, pp. 7–13.
[44] Eisenlohr, P. and W. Blum. Bridging steady-state deformation behavior at low and high temperature by considering dislocation dipole annihilation. *Materials Science and Engineering A*, Vol. 400–401, 2005, pp. 175–181.
[45] Perić, M., Z. Tonković, A. Rodić, M. Surjaka1, I. Garašić, I. Borasa, et al. Numerical analysis and experimental investigation of welding residual stresses and distortions in a T-joint fillet weld. *Materials & Design*, Vol. 53, 2014, pp. 1052–1063.
[46] Yonetani, S. *The generation of residual stress and countermeasures*, China Machine Press, Beijing, CN, 1983.

[47] Chen, X. Y., L. H. Zhan, Z. Y. Ma, Y. Q. Xu, Q. Zheng, and Y. X. Cai. Study on tensile/compressive asymmetry in creep ageing behavior of Al–Cu alloy under different stress levels. *Journal of Alloys and Compounds*, Vol. 843, 2020, id. 156157.

[48] Deschamps, A., F. Livet, and Y. Brechet. Influence of predeformation on ageing in an Al–Zn–Mg alloy—I. Microstructure evolution and mechanical properties. *Acta Materialia*, Vol. 47, No. 1, 1998, pp. 281–292.

[49] Deschamps, A. and Y. Brechet. Influence of predeformation and ageing of an Al–Zn–Mg alloy—II. Modeling of precipitation kinetics and yield stress. *Acta Materialia*, Vol. 47, No. 1, 1998, pp. 293–305.

[50] Wagner, R., R. Kampmann, and P. W. Voorhees. Homogeneous second phase precipitation. *Phase transformations in materials science and technology*, 1st edn. G. Kostorz, Ed, Wiley-VCH Verlag GmbH, Weinheim, 2001, pp. 309–407.

[51] Flynn, C. P. *Point defects and diffusion*, Oxford University Press, NewYork, US, 1972.

[52] Mura, T. *Micromechanics of defects in solids*, Springer, Dordrecht, NL, 1987.

[53] Zhu, A. W. and Starke, Jr E. A. Stress aging of Al–Cu alloys: computer modeling. *Acta Materialia*, Vol. 49, No. 15, 2001, pp. 3063–3069.